Broadband X-ray Detector Using CCDs and Scintillators

Emi Miyata
Department of Earth and Space Science, Graduate School of Science, Osaka University
1-1 Machikaneyama, Toyonaka, Osaka 5600043 JAPAN

We report on a new photon-counting detector, scintillator directly-coupled CCD (SD-CCD), possessing unprecedented spatial resolution and moderate spectral resolution for 0.1-100 keV X-rays. The SD-CCD consists of an X-ray charge-coupled device (CCD) and a scintillator. The scintillator is directly coupled to the back surface of the X-ray CCD. Low-energy X-rays below 10 keV can be directly detected by the CCD. The majority of hard X-rays above 10 keV pass through the CCD but can be absorbed by the scintillator, generating visible photons. Since CCDs have a moderate detection efficiency, visible photons can be detected by the CCD. We employed the needlelike CsI(Tl) for scintillators in order to obtain high spectral resolution as well as high spatial resolution. We performed the Monte Carlo simulation to optimize the needlelike CsI(Tl) as an X-ray spectrometer. We found that fine needle structure with diameter of 5 μm deposited on the plate reflectively coated enables us to improve the spectral capability. It is found to be essential that the material with refractive index of $1.65-1.7$ is filled between each needle as deep as possible to improve the spectral capability.
We fabricated the optimized 300 μm thick needlelike CsI(Tl) and coupled it on the front surface of the back-illuminated (BI) CCD. High detection efficiency for visible photons of the BI CCD enables us to collect visible photons emitted from CsI(Tl) efficiently. We measured the hard X-ray responsivities of the newly developed SD-CCD with monochromatic X-ray beam for $20-80$ keV. The excellent linear relationship is obtained between the incident X-ray energy and the peak pulse height. The energy resolution depends on the inversely square-root of energy. For the astrophysical application, we will perform the balloon-born experiment of the hard X-ray observation with hard X-ray focusing telescope, Supermirror, in October 2006 at Brazil.

1. INTRODUCTION

Current and past X-ray observatories carry grazing incidence X-ray telescopes coated with high-Z materials (such as gold or iridium), enabling focusing of photons with energies below 10 keV. It is difficult to focus X-rays above 10 keV since the total external reflection at these energies occurs at extreme grazing incidence ($\leq$0.1 degree). A big breakthrough in X-ray astronomy has brought by the hard X-ray focusing optics, supermirror [1, 2]. The supermirror possesses a depth-graded multilayer structure in order to achieve high reflectivity in a wide energy band. Essentially, the multilayer acts as an X-ray reflector. Its periodic structure can reflect X-rays which satisfy the Bragg condition, like a crystal. The Bragg angle is determined by the periodic length of the structure, and it is much larger than the critical angle needed for the total external reflection of light. Since the hard X-ray telescope is required to have high throughput, multinested optics made from thin substrates are the most suitable for use with the supermirror. The spatial resolution of such optics is expected to be $\sim$15 arcsec (half power diameter), achieved with the *XMM-Newton* satellite [3].

The focal plane detector for the supermirror is required to cover the energy range of $0.1-100$ keV with an imaging capability of several arcseconds for, at least, a 15 arcmin square region. Due to their moderate spectral resolution with excellent imaging capability in the $0.1-10$ keV band, charge-coupled devices (CCDs) are now widely employed as focal plane detectors on recent X-ray satellites such as *ASCA* [4], *Chandra* [5], and *XMM-Newton* [3]. Since CCDs are made of silicon, the stopping power for hard X-rays significantly drops above the 10 keV energy range.

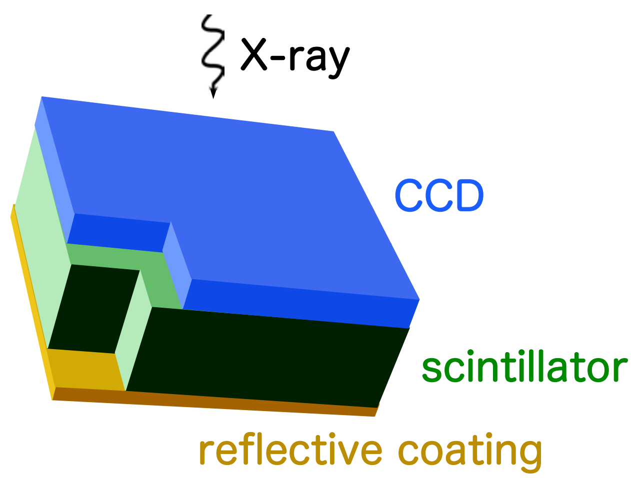

Figure 1: Design concept of the SD-CCD. The scintillator is directly coupled to the back surface of the CCD which enables us to collect high-energy X-rays in the scintillator. Since CCD possesses the high detection efficiency for visible photons, visible photons generated in the scintillator can be detected by the same CCD.

2. NEW X-RAY DETECTOR

We report here a newly developed wide-band photon-counting detector for $0.1-100$ keV X-rays possessing high spatial resolution, to be employed as the focal plane detector of a hard X-ray telescope: the scintillator directly-coupled CCD (SD-CCD). The design concept of the SD-CCD is shown in Fig. 1. We employ the CCD itself as a soft X-ray detector. The scintillator is directly coupled to the back surface of the CCD. The majority of X-rays having energy of above 10 keV cannot be absorbed by the CCD and pass through it. However, they can be absorbed by the scintillator and emit hundreds or thousands of visible photons. The visible scintillation photons can be absorbed by the same CCD. In order to maximize the number of visible photons detected by CCDs, the surface of the scintillator is coated by a reflector, such as aluminum, which leads to a better energy resolution.

The shape of the charge cloud generated by X-rays directly detected in BI CCDs has already been investigated [6]. Its size decreases with the mean absorption length in silicon and ranges from 2.5$\sim$4.5 μm for 1.5$\sim$4.5 keV X-rays. The size of the charge cloud generated by X-rays above 4.5 keV is roughly constant because of thin depletion depth [7]. On the other hand, photons emitted from the scintillator expand uniformly in the first approximation and the size of their extent is expected to be roughly the thickness of the scintillator. The difference of sizes between the charge clouds generated by X-rays directly absorbed by the CCD and those by X-rays absorbed by the scintillator enables us to distinguish the two kinds of X-ray events. This suggests that the SD-CCD can function as a photon-counting detector for $0.1-100$ keV X-rays. Currently, there is no other photon-counting detector available for such a wide energy band.

The thicker the scintillator, the better is the detection efficiency. However, the extent of visible photons becomes larger for a thicker scintillator, resulting in poorer identification of the X-ray point of interaction. Moreover, the large extent of visible photons affects the pile-up of X-rays directly detected by CCDs. Therefore, it is important to confine the extent of visible photons. There is a promising scintillator, CsI(Tl), which not only possesses one of the highest light yields among scintillators [8] but also forms a needlelike fine crystal structure that resembles optical fibers [9]. Figure 2 shows the photograph of the needlelike CsI(Tl) obtained with the scanning electron microscope (SEM). The mean diameter of each needle is roughly 5 μm. The needlelike structure significantly reduces the lateral spread of visible photons and prevents the image from being degraded, thus assuring even higher sensitivity. Hard X-ray detectors employing the needlelike scintillators have already been proposed (e.g. [10–12]) but no other detectors can detect soft X-rays and are operated in a photon-counting mode.

Miyata & Tamura [13] demonstrated the photon-counting capability for hard X-ray regions with the scintillator-coupled CCD for the first time. Miyata et al. [14] have developed the deposition of the needlelike CsI(Tl) directly on the CCD and fabricated the SD-CCD. The needlelike structure of the scintillator

Figure 2: SEM photograph of the surface structure of the needlelike CsI(Tl). The top of each needle has a sharp edge structure. The horizontal bar located at the bottom corresponds to 10 μm.

prevents the lateral spread of visible photons emitted from the scintillator. They deposited the CsI(Tl) on the backside of the BI CCD, the side closest to the electrodes. Since this configuration essentially operates the CCD in a front-illuminated mode, we refer to this device as SD-FICCD. Due to its low detection efficiency of the front side, $\sim$80% of visible photons are absorbed both by the electrodes and by the covering material. They operated the SD-FICCD with the nominal operation of the CCD and found that events generated by visible photons emitted from CsI(Tl) are too weak to be identified. They operated the SD-FICCD with the on-chip binning mode by 2×2 and 4×4 pixels, resulting in significant improvements in the collection efficiency of charge generated by visible photons. However, the on-chip binning mode reduced the imaging capability because the effective pixel size increased. The increase of the effective pixel size also caused the increase of noise generated by the dark current, resulting in poorer spectral capability than that without the on-chip binning.

Miyata et al. [15] fabricated the SD-CCD employing the front side of the BI CCD to collect visible photons emitted from CsI(Tl). We refer to this new type of SD-CCD as SD-BICCD-100. The peak wavelength of emitted spectra of CsI(Tl) is 550 nm. The detection efficiency at the front side of the BI CCD is more than 85% at 550 nm four times better than that of the backside of the BI CCD. We, therefore, expect high detection efficiency of visible photons emitted from CsI(Tl). They demonstrated the high X-ray responsivity of the SD-BICCD-100. The energy resolution at full-width of half maximum (FWHM) is 28.4% at 22.1 keV and 25% at 59.5 keV. However, the thickness of CsI(Tl) employed is 100 μm, resulting the detection efficiency at 60 keV to be 29%. Miyata et al. [16] measured hard X-ray responsivities of the SD-BICCD-100 at the largest third-generation synchrotron radiation facility, SPring-8, located at Hyogo, Japan. They found an excellent linearity between the incident X-ray energy and the peak pulse height for 20−80 keV X-rays. The energy resolution depends inversely on the square-root of the X-ray energy.

In this paper, we develop thick needlelike CsI(Tl) in order to improve the detection efficiency. When the thickness of CsI(Tl) increases, the number of visible photons emitted might decrease as decreasing the X-ray absorption depth as well as increasing the spread of visible photons. We therefore performed the Monte Carlo simulation to optimize the structure of the needlelike CsI(Tl). Then we fabricate the SD-CCD with the optimized needlelike CsI(Tl) and evaluated the X-ray responsivity.

3. SIMULATIONS

We performed the Monte Carlo simulation with DETECT2000 [17, 18]. DETECT2000 is a Monte Carlo simulation program that tracks individual visible photons inside a simulation model and records the fate of each one. The model geometry is defined as a collection of simple geometric shape such as plane and cylinders. Many surface finishes are available to create a more accurate simulation model. BUILDER is a program that comes with the DETECT2000 suite whereas the geometry can be made with BUILDER is not enough to simulate the geometry we need. We thus develop the custom program with the `perl` script to construct the complex geometry we need.

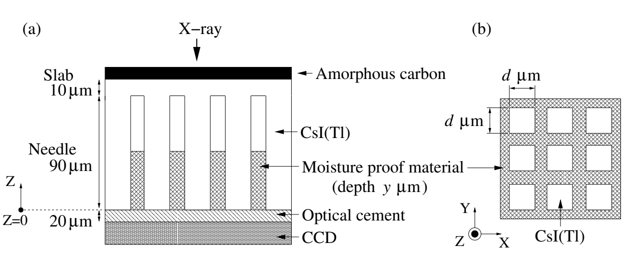

Figure 3: The modeled geometry of SD-CCD which coupled the 100 μm thick needlelike CsI(Tl) with optical cement. (a) The cross-section of the SD-CCD in parallel with the CCD surface. (b) The cross-section of the SD-CCD in vertical to the CCD surface. The needlelike CsI(Tl) is depth of 90 μm and the slab structure is depth of 10 μm, therefore the total depth of CsI(Tl) is 100 μm.

3.1. Geometry

Figure 3 shows the cross-section of the SD-CCD we modeled and the definitions of axis. The needlelike CsI(Tl) we employed is deposited on the amorphous carbon plate [9]. The diameter of each needle is about 5 μm as shown in Fig. 2 and we set it to be a free parameter (d μm) for simulation. The size of each needle is $d \times d \times Z$ μm^3 , each of which is separated by a 1 μm. We assume the 10 μm thick slab CsI(Tl) at the bottom of the needlelike CsI(Tl). After deposition, the moisture proof material is deposited from the top of the needlelike CsI(Tl) whereas it cannot reach the bottom of the needle. The moisture proof material is assumed to be filled between each needle to the depth of y μm. Then we couple it to the CCD with the optical cement to construct the SD-CCD. The top of needle is coupled to the surface of the CCD with the optical cement. The thickness of the optical cement is fixed at 20 μm. The values of refractive index for CsI(Tl), optical cement, moisture poof material and amorphous carbon are 1.79, 1.57, ∼1.6, and 2.3 [19], respectively.

3.2. Simulation Basis

We assumed an X-ray is absorbed in the needlelike CsI(Tl) and generate 10000 visible photons there. The X-ray absorption is occurred at the center of the needle in X-Y plane. We construct 498×498 μm^2 area where there are 83×83 needlelike crystals. The visible photons generated are reflected or refracted in the surface of each needle until they are absorbed by the CCD, absorbed in the amorphous carbon or escape from the SD-CCD. There is no data of optical transmittance available for the needlelike CsI(Tl). We here assume the the mean free path of CsI(Tl) for visible lights to be same as that of conventional non-needlelike CsI(Tl) of 1000 mm. Since this value is much larger with the thickness of each needle, we ignore the absorption within the CsI(Tl).

We calculate the number of visible photons integrating over the area of 480 μm square on the CCD in the case that visible photons are generated at depth Z of 5∼95 μm with 5 μm step. We assume the quantum efficiency of the CCD to be 100% for visible lights.

3.3. Tuning of Simulation

Since the surface roughness of the needlelike crystals is difficult to measure, we determined it in order to obtain consistency with experimental results. We modeled the surface roughness with an "UNIFIED" model of DETECT2000 suite. This model assumes that the angle between the local micro-facet normal and the average surface normal follows a Gaussian distribution with a standard deviation (SD). Hence SD

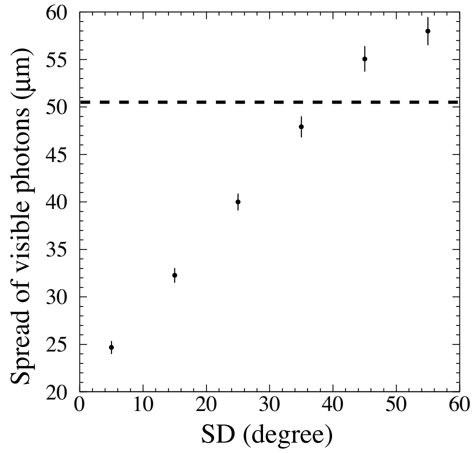

Figure 4: Spread of visible lights of the needlelike CsI(Tl) as a function of SD. The dashed line shows the values obtained with the SD-BICCD-100 of 50.6 μm.

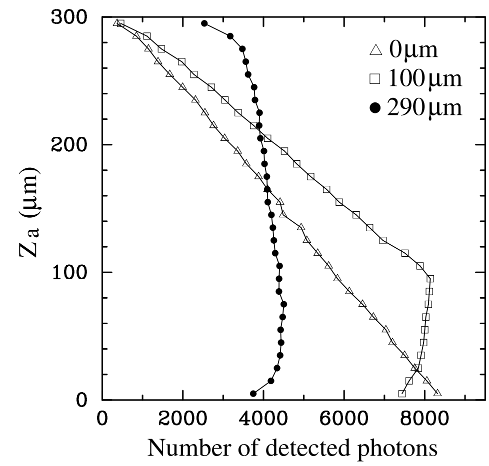

Figure 5: Correlation between the absorption depth of X-ray photon , Z_a, and the number of visible photons detected for y of 0, 100, and 290 μm. The initial number of visible photons was 10000.

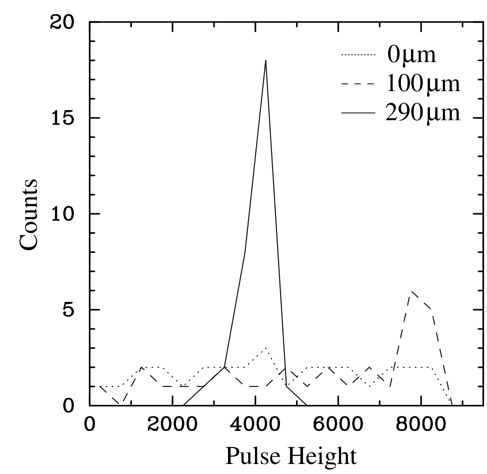

Figure 6: Simulated spectrum for y of 0, 100, and 290 μm.

shows the roughness of a surface. We assume other parameters of the simulation as the design value or experimental values.

We calculated the spread of visible photons appeared on the CCD and compared it with the experimental results obtained with the SD-BICCD-100 [15]. Since the absorption depth of X-rays are distributed as their mean absorption depth, we calculate the spread of visible photons (F_w) weighted by the X-ray absorption depth.

Figure 4 shows F_w as a function of SD for 59.5 keV X-rays. The values of F_w linearly increases with the values of SD and saturates for SD>50° because of limited thickness of CsI(Tl). The F_w obtained with the SD-BICCD-100 was (50.6±0.3) μm at 59.5 keV which can be realized with SD of 35°. We thus employed SD of 35° as the surface roughness of needlelike CsI(Tl).

3.4. Optimization of Needlelike CsI(Tl)

We thus verified we could reproduce our experimental results obtained with the SD-BICCD-100 by the Monte Carlo simulation of DETECT2000. Based on the results of 100 μm thick CsI(Tl), we optimized the structure of 300 μm thick CsI(Tl).

3.4.1. Depth of Moisture Proof Material

We first optimized the depth (y) of the moisture proof material in needlelike CsI(Tl). The moisture proof material is coated on CsI(Tl) in order to keep water off the CsI(Tl) and prevent the spread of visible lights emitted from CsI(Tl). Since the aperture ratio of the needlelike structure is high, it is relatively difficult to fill the moisture proof material deep in CsI(Tl).

Figure 5 shows the correlation between Z_a and the number of visible photons detected for y of 0, 100, and 290 μm. As clearly shown in this figure, the spread of the number of visible photons along the depth increases with decrease of y. For y=0, no moisture proof material fills between needles and the critical angle for visible lights emitted from needles is 32°. On the other hand, when there is a moisture proof material between needles, the critical angle is 53°. Therefore, the number of photons collected by the total reflection is larger for y=0 than for y=290 whereas the number of reflections for y=0 is larger than those for y=290. Since the surface roughness of the needlelike CsI(Tl) is relatively large as shown in Fig. 4, the increase in the number of reflections on the needle surface results in the increase of the number of visible photons lost by scatter, leading the increase of the spread of visible photons on the CCD. When we integrate the limited area on the CCD, the number of photons collected decreases as increase of the number of total reflections seen in y=0 in Fig. 4. In the case of y=290, the number of photons collected is essentially limited by the total reflection angle of 53°, leading to the small number of visible photons collected but no dependence on Z_a.

The energy resolution of spectrum depends both on the mean number of visible photons and on the variation of the number of visible photons along the depth. In the case of y=290 μm, the number of visible photons are relatively small whereas its number is independent on Z_a. Figure 6 shows the spectrum expected for y of 0, 100, and 290 μm. We can estimate the incident X-ray energy only for y=290 μm.

Based on this simulation, we confirm that the coating around the needlelike CsI(Tl) is essential to obtain the high energy resolution. For the next step, we performed the simulation to optimize the refractive index of the moisture proof material.

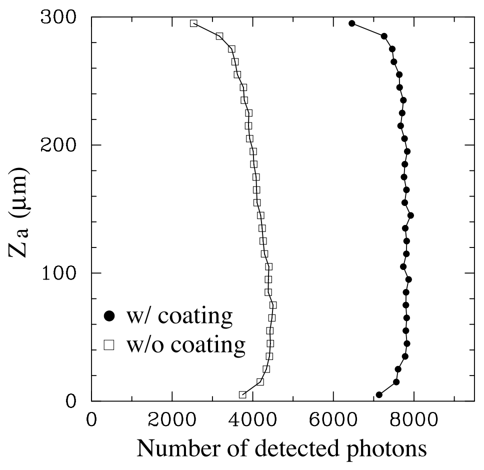

Figure 7: Same as Fig. 5 but for the amorphous carbon plate with and without the reflective coating on the amorphous carbon plate. The reflectivity of the metal coating is assumed to be 90%.

3.4.2. Reflective coating

We deposited the needlelike CsI(Tl) on the amorphous carbon plate. Since the surface of the amorphous carbon plate is black, the majority of visible lights coming to the plate are absorbed. We thus investigate the possible improvement of the reflective coating for the surface of amorphous carbon plate. Figure 7 shows the correlation between Z_a and the number of visible photons detected by the CCD with and without the reflective coating of the amorphous carbon plate. The reflective coating enables us to increase the number of visible photons collected by the CCD by a factor of two. We thus confirmed reflective coating of the amorphous carbon plate is essential to increase the number of visible photons detected by the CCD, leading to improve the spectral capability.

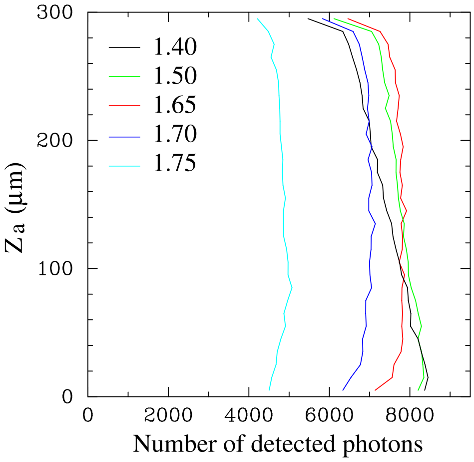

Figure 8: Same as Fig. 5 but for refractive index of the moisture proof material of 1.40, 1.50, 1.65, 1.70, and 1.75.

3.4.3. Moisture Proof material

We next optimized the refractive index of moisture proof material. We simulated the number of visible photons detected by the CCD for various moisture proof material having different refractive indices. Figure 8 shows the correlation of the number of visible photons detected by the CCD for moisture proof material having refractive index of 1.40, 1.50, 1.65, 1.70, and 1.75. In the case of small refractive index of 1.40, the number of photons decreased with increasing depth in CsI(Tl). This is because the critical angle increases with increase of the refractive index. The variation of the number of visible photons are relatively constant for refractive index $\geq$ 1.65.

In order to obtain a high spectral capability, the refractive index of the moisture proof material needs to be in ranges of 1.65$\sim$1.7. So, we confirmed that the current material employed for the moisture proof having the refractive index of $\sim$1.6 has already optimized to obtain high spectral capability.

3.4.4. Diameter of needle

We then optimized the diameter of needlelike CsI(Tl). We calculated the correlation of the number of visible photons detected by the CCD for the diameter of needlelike CsI(Tl) of 5, 10, and 20 μm as shown in Fig. 9. As clearly shown in this figure, the smaller diameter results in a higher number of the visible photons detected by the CCD. We again confirmed that the current design value of 5 μm has already optimized to obtain high spectral capability and fixed the diameter of the needle to be 5 μm.

4. DEVICES

Based on the simulation results, we fabricated 300 μm thick needlelike CsI(Tl) on the reflective

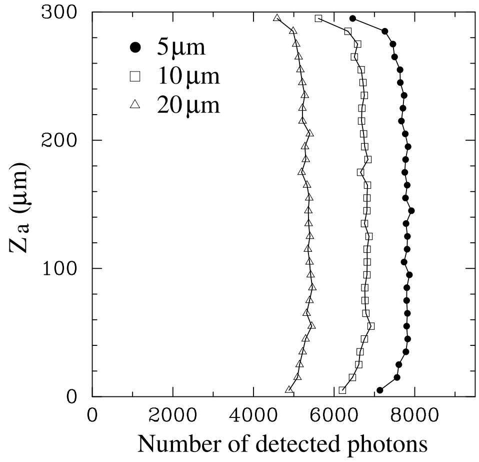

Figure 9: Same as Fig. 5 but for diameter of each needle of 5, 10, and 20 μm.

coated amorphous carbon plate. The diameter of needles was $\sim$5 μm. The moisture proof material with the refractive index of $\sim$1.6 was filled as deep as possible. We then coupled it on the front surface of the BI CCD with the optical cement to develop the SD-CCD. We refer to this new type of SD-CCD as SD-BICCD-300. The BI CCD employed is "S7170-0909" fabricated by Hamamatsu Photonics K.K. and has 512$\times$512 pixels each 24 μm square. The BI CCD is etched from the back toward the depletion layer in order to achieve high detection efficiency for blue light and low-energy X-rays [20]. At the end of this thinning process, almost all of the substrate has been removed and the thickness of the BI CCD is 35 μm. The wafer of the BI CCD is "epitaxial-3" whose depletion layer is estimated to be 35 μm when we apply a gate voltage of 4 V in the imaging area [21]. Since the wafer thickness is 35 μm, this BI CCD can be operated in a full-depletion operation [7]. The full-depletion operation is essential in order not to expand the lateral spread of visible photons caused by the diffusion process in the field-free region inside the CCD.

5. EXPERIMENTS

5.1. Experimental Setup

For measurements of the system gain and the readout noise, ^{55}Fe was used to irradiate the CCD before it was coupled with the CsI(Tl). We operated the BI CCD with the *MiKE* system [22] which was developed for operation of conventional CCDs and possesses excellent low noise performance. The analog data were processed by an integrated correlated double-sampling circuit [21] which was also developed for conventional CCDs. The readout noise level was evaluated by a histogram of the horizontal over-clocked region and was 4 e$^-$ including the CCD. It should be noted that the operation and the data acquisition method of the SD-CCD is essentially the same as those of conventional CCDs. Therefore, we need to develop no extra electronics for the SD-CCD. We confirmed that there was no change in the readout noise after coupling the CsI(Tl).

In order to reduce the thermal noise of the CCD, the device was maintained at $-60\,^\circ$C during the experiment. The light yield of CsI(Tl) at $-60\,^\circ$C is $\sim$60 photons/keV [8].

5.2. Hard X-ray Responsivity of SD-BICCD-300

We evaluated the hard X-ray responsivity of the SD-BICCD-300 at SPring-8. The beamline BL20B2 we employed is the bending-magnet beamline and is developed for medical applications and various imaging techniques. The BL20B2 consists of an optics hutch and three experimental hutches. A fixed-exit double crystal monochromator is located in the optical hutch and enables us to irradiate a monochromatic X-ray beam from 8.4 to 72.5 keV with Si(311) and from 13.5 to 113.5 keV with Si(511). The second and third experimental hatches are located 200 and 206 m away form the source point. The SD-BICCD-300 was installed in the third hutch.

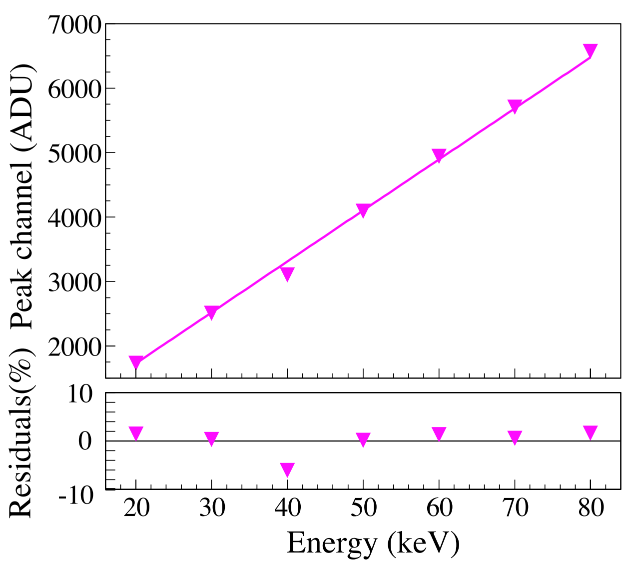

Figure 10: Energy dependence of pulse height obtained with the SD-BICCD-300. We extracted them with the Lorentzian function. The solid line shows the best-fit linear function and the lower panel shows residuals between data and model.

We irradiated the monochromatic X-ray beam of 20, 30, 40, 50, 60, and 70 keV with Si(311) and 80 keV with Si(511) to the SD-BICCD-300. The X-ray mirror coated by Pt 1000 Å was employed for 20$-$60 keV

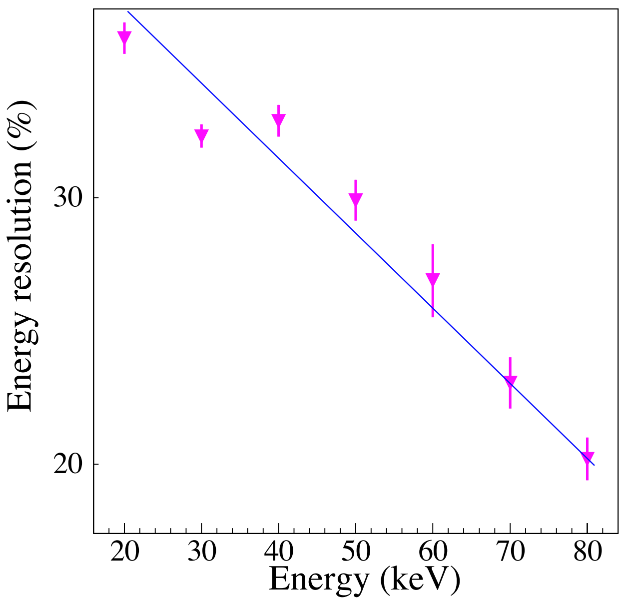

Figure 11: Energy dependence of the energy resolution obtained with the SD-BICCD-300. The solid line shows the inverse square-root of energy function.

beam in order to eliminate higher harmonics. We operated the SD-BICCD-300 with an on-chip binning mode by 4×4 pixels [15]. Even if we operated the SD-BICCD-300 with the on-chip binning mode, the cluster size of each event was 3×3 pixels or more extended. Therefore, each 5×5 pixel region of a frame is sequentially scanned for X-ray event extraction. A pulse height of the central pixel among 5×5 pixels is compared with a threshold, so called an event threshold. The event threshold is set to be 4 times the readout noise. If a pulse height of the central pixel is equal to or larger than the event threshold, its value is compared with those of neighboring 8 pixels whether it is a local maximum among central 3×3 pixels or not. If the local maximum is found, 5×5 pixels centered at the local maximum is considered as an event. The central pixel of 5×5 pixels is assumed to be an X-ray point of interaction. We then fitted the spatial distribution of pulse height of 5×5 pixels with a Lorentzian function and extracted the pulse height as an integration of the best-fit model.

Figure 10 shows the pulse height as a function of X-ray energy. The linear relationship between the incident X-ray energy and the pulse height can be obtained with a maximum deviation from a linear function of 6% at 40 keV which is just above the K absorption edges of Cs and I.

Figure 11 shows the energy resolution in FWHM as a function of X-ray energy. The energy resolution depends on the inversely square-root of energy, suggesting that the energy resolution is limited by the statistics of visible photons emitted from CsI(Tl). The energy resolution at 80 keV is 20±1% which is comparable to that obtained with the conventional scintillation counter.

The peak pulse height obtained with the SD-BICCD-300 is roughly twofold that with the SD-BICCD-100 [16]. This demonstrates that the reflective coating of the amorphous carbon plate enables us to improve the photon collection efficiency significantly. The energy resolution obtained with the SD-BICCD-300 is comparable to or slightly better than that with the SD-BICCD-100 in spite of the thicker CsI(Tl). We thus confirm that we can optimize the structure of needlelike CsI(Tl) to infer the high spectral capability with DETECT2000. We can demonstrate that the SD-CCD can surely function as a X-ray spectrometer from 20 to 80 keV.

5.3. Imaging Capability

We measured the on-axis image of the supermirror with the SD-BICCD-300. The supermirror we employed was recovered from the third flight of InFOCμS balloon-borne experiment. The optics is conically approximated Wolter-I with aperture diameter of 400 mm and focal length of 8000 mm. The supermirror consists of four quadrants, each of which has 255 nested thin Al reflectors. Details about the supermirror can be found elsewhere [23].

The experiment was also performed at the beamline BL20B2 of SPring-8. The supermirror was installed in the second hutch and the separation between the supermirror and the SD-BICCD-300 was set to be 8000 mm. We employed 40 keV monochromatic X-rays with beam size of 10 mm×10 mm in order to obtain a parallel X-ray beam. The supermirror was therefore scanned with such a small X-ray beam. We scanned the supermirror having a radius of $\leq$110 mm since the outer region of the supermirror could not be scanned because of experimental setup. In total, 1278 scans were performed. It should be noted that the reflectivity of supermirror decreases as increasing radius especially for hard X-rays. Therefore, our results does not change significantly if we scan the whole area of the supermirror.

The SD-BICCD-300 was operated in a photon-counting mode and five frame data were obtained at each position. Figure 12 shows the on-axis image of the supermirror at 40 keV. The sharp core and the wing structure of the supermirror can be clearly imaged with the SD-BICCD-300. This image can demonstrate the high imaging capability of the SD-BICCD-300.

6. CONCLUSION

We have developed the new type of SD-CCD (SD-BICCD-300) by coupling 300 μm thick CsI(Tl) on the

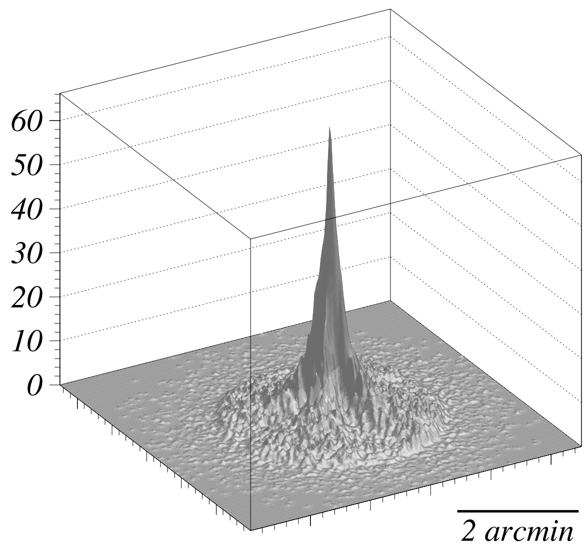

Figure 12: On-axis image of the supermirror measured at 40 keV with the SD-BICCD-300.

front surface of the BI CCD . We evaluated the hard X-ray responsivity at the synchrotron radiation facility. The SD-BICCD-300 can function as a spectrometer for hard X-rays from 20 to 80 keV both with a high linearity and with a moderate energy resolution. We measured the on-axis image of the supermirror at 40 keV. Both the sharp core and the wing structure can clearly be imaged with the SD-BICCD-300 and we can demonstrate the high imaging capability of our device.

For the astrophysical application, we will perform the balloon-borne hard X-ray experiment, SUMIT, jointly developed by Nagoya University and ISAS/JAXA [24]. The first SUMIT flight will be performed at Brazil in October 2006 with an international collaboration with INPE in Brazil.

Acknowledgments

We acknowledge the support from the CCD group of Osaka University and from Hamamatsu Photonics K.K. We thank Drs. K. Uesugi, Y. Ogasaka, K. Tamura and R. Shibata for collaboration of the balloon experiment as well as the experiment at SPring-8 BL20B2. The hard X-ray measurements were performed at the BL20B2 in the SPring-8 with the approval of the Japan Synchrotron Radiation Research Institute (JASRI) (Proposal No. 2004A0009-LM-np). This work is partly supported by Grants-in-Aid for Scientific Research from the Ministry of Education, Culture, Sports, Science and Technology (16002004). This study is also carried out as part of the 21st Century COE Program, '*Towards a new basic science: depth and synthesis*'.

References

[1] K. Yamashita et al., Applied Phys. 37, 8067-8073, 1998.

[2] K. Tamura et al., Proc. SPIE, 4851, 1048-1058, 2003.

[3] P. Barr et al., ESA SP-1097 1988.

[4] Y. Tanaka, H. Inoue, and S. S. Holt, Publ. Astron. Soc. Jpn. 46, L37-L42, 1994.

[5] M. W. Bautz, J. A. Nousek, G. P. Garmire, *Science Instrument Calibration Report for the AXAF CCD Imaging Spectrometer (ACIS)*, 1999.

[6] E. Miyata, M. Miki, J. Hiraga, H. Kouno, K. Yasui, H. Tsunemi, K. Miyaguchi and K. Yamamoto, Jpn. J. Appl. Phys. 41, 5827-5834, 2002.

[7] E. Miyata, M. Miki, D. Kamiyama, H. Tsunemi, and K. Miyaguchi, Jpn. J. Appl. Phys. 42, 7135-7139, 2003.

[8] J. D. Valentine, D. K. Wehe, G. F. Knoll and C. E. Moss, IEEE Trans. Nucl. Sci. 40, 1267-1274, 1993.

[9] *FOS (Fiber Optic Plate with Scintillator) for Digital X-ray Imaging*, Hamamatsu Photonics Technical Information, 1996.

[10] V.V. Nagarkar, J.S. Gordon, S. Vasile, P. Gothoskar, and F. Hopkins, IEEE, Trans. Nucl. Sci. 43, 1559-1563, 1996.

[11] V.V. Nagarkar et al., IEEE, Trans. Nucl. Sci. 46, 232-236, 1999.

[12] V.V. Nagarkar et al., IEEE, Trans. Nucl. Sci. 50, 297-300, 2003.

[13] E. Miyata and K. Tamura, Jpn. J. Appl. Phys. 42, L1201-L1204, 2003.

[14] E. Miyata, M. Miki, N. Tawa and K. Miyaguchi, Jpn. J. Appl. Phys., 44, 1476-1484, 2005.

[15] E. Miyata, N. Tawa, K. Mukai, H. Tsunemi, and K. Miyaguchi, IEEE Trans. Nucl. Sci. 53, 576-583, 2006.

[16] E. Miyata, N. Anabuki, K. Mukai, N. Tawa, T. Miyauchi, H. Tsunemi, and K. Miyaguchi, Nucl. Instrum. & Methods A in press 2006.

[17] G.F. Knoll, T.F. Knoll, T.M. Henderson, IEEE Tran. Nucl. Sci. 35, 872-875, 1988.

[18] G. Tsang, C. Moisan, J.G. Rogers, IEEE Tran. Nucl. Sci. 42, 2236-2243, 1995.

[19] W. W. Duley, ApJ, 287, 694, 1984.

[20] M. Muramatsu, H. Akahori, K. Shibayama, S. Nakamura and K. Yamamoto, Proc. SPIE, 3019, 2-8, 1997.

[21] E. Miyata, C. Natsukari, T. Kamazuka, H. Kouno, H. Tsunemi, M. Matsuoka, H. Tomida, S. Ueno, K. Hamaguchi and I. Tanaka, Nucl. Instrum. & Methods A, 488, 184-190, 2002.

[22] E. Miyata et al. Proc. SPIE in press 2006.

[23] R. Shibata et al. Proc. SPIE, 5488, 313-324, 2004.

[24] H. Kunieda et al. Proc SPIE in press 2006.